Journal of
Renewable Energy Research and Applications (RERA)

Vol. 4, No. 1, 2023, 87-101 *DOI: 10.22044/rera.2021.11214.1081*

Reinforcing Proton Exchange Membrane Fuel Cell Powered Unmanned Aerial Vehicle with an Innovative Combined Flow Field

M. Rostami, A. Farajollahi*, F. Bagherpor and V. Sfandiyari

Department of Aerospace Engineering, Faculty of Engineering, Imam Ali University, Kargar Street, Tehran, Iran.

Received Date 15 September 2021; Revised Date 16 October; Accepted Date 18 October 2021
**Corresponding author: a.farajollahi@sharif.edu (A. Farajollahi)*

Abstract

Polymer electrolyte membrane fuel cells (PEMFCs) can be the main part of the ideal propulsion system of Unmanned Aerial Vehicles (UAVs) due to the high power density and suitable efficiently. Flow fields play a key role in the performance of PEMFC-powered UAVs. In this work, a novel flow field named modified combined is introduced in order to reinforce the performance of the UAV propulsion system. The flow field is investigated by a 3D and two-phase PEMFC model. In the flow field, the main channels are tapered aiming to reduce the pressure drop and prepare a suitable water management. This work consists of two steps. In the first stage, the modified combined is compared with the parallel, serpentine, interdigitated, and combined. The results obtained show that in the modified combined compared with the simple combined, the pressure drop decreases to22.6%. The modified combined demonstrates a suitable oxygen distribution and an appropriate water management. Furthermore, among all the flow fields, the specific power of the modified combined is the highest. Finally, the effect of the atmospheric conditions on the performance of PEMFC with the modified combined flow field is studied, and two equations are presented to in order predict the performance at 0.4V and 0.7V at different flight altitudes. The equations unveil the point that although the increase of height at high reduces the output power especially at the low voltage, the specific power at 0.4 V is higher. Therefore, in the cruise phase of the flight, a low voltage is more suitable for PEMFC-driven UAV with a modified combined flow field. All in all, the modified combined flow field and low voltage are recommended to be utilized in PEMFCs as the propulsion system of UAVs.

Keywords: *PEMFC; Innovative flow field; Atmospheric conditions of flight; Performance.*

1. Introduction

Unmanned aerial vehicles (UAVs) are aircrafts that are designed to operate without a pilot on board [1]. The significance of some complicated missions that are inadaptable for human constraint organizations is to employ UAVs due to their safety, durability, and efficiency [2].

UAVs utilize a battery or a Polymer Electrolyte Membrane Fuel Cell (PEMFC) or an internal combustion engine or a combination of them as their propulsion system[1]. The fuel cell provides the two advantages of increasing endurance and providing secrecy according to the low operating temperature so the tendency to use PEMFCs in UAVs has been prompted[3]. A PEMFC system has a lower specific fuel consumption since it produces the required power in a non-combustion process.

According to the advancement of PEMFCs, many efforts have been dedicated in order to improve this amazing technology. Some studies have focused on the water and heat management [4,5], clamping pressure [6], channel geometry [7],and the effect of baffles[8]. Various kinds of flow field designs have been presented including parallel, serpentine, combined, and interdigitated [9],and investigated under different operating conditions [10].

Flow fields in the fuel cell play a vital role in the transport of reactants and reaction products, and is an important factor in determining the power of the fuel cell. Increasing the cell power is very effective in increasing the performance capability of the drone. By modifying the fuel cell flow field, the cell power can be increased. In a study carried out by Afshari and Ziaei Rad [11], an innovative zigzag-shaped flow channel has been proposed for the cell cooling flow field. The results obtained showed that in a cell with a trapezoidal cross-section, the maximum surface temperature, temperature uniformity index, and

cooling temperature were lower than a similar cell with a rectangular cross-section. Ghasabehi et al. [12]have introduced a novel tapered parallel flow field. The flow field not only increased the output power density but also decreased the pressure drop and enhanced the water management. Devi et al. [13]have proposed a new design for the flow field. They added sub-channels to the flow field, and compared a serpentine flow field with the sub-channel and a conventional serpentine flow field. The results obtained showed that due to the improvement of the current under the rib of the flow field with the sub-channel, the maximum current density and the power density increased by18.85% and 23.74%, respectively. In another numerical study, using the computational fluid dynamics, the effect of baffle number and height along flow channels has been studied by Heidari et al. [14]. The findings showed that the complete blockage of cathode-side flow channels with 5 blocks increased the net power by 30%. Fan et al. [15]have optimized the geometric properties of the baffle. They found that the highest cell performance was achieved with baffles at an angle of 30 degrees and a width of 5 mm and a distance of 6 mm from each other. Mehrdad Ghasabehi et al. [12]have suggested a modified tapered parallel flow field enhanced uniformity of current density, reactant transport, and water management, resulting in a higher generated power and a lower pressure drop.

One of the significant parameters involved in the cell performance is the dimensions of the flow field. Yang et al. [16] have optimized the dimensions of the channel and rib by the genetic algorithm. This optimization stated that the channel width to rib ratio of 2.8 to 0.5 and 4.2 to 0.3 showed the ideal efficiency. Wang et al. [17]have numerically studied the effect of channel size on the cell performance with a serpentine flow field. The results obtained showed that a smaller channel size improved the removal of liquid water and increased the output power of the cell but at the same time increased the work of the pump. The optimal dimensions for the channel cross-section are 0.535 mm by 0.535 mm. In a numerical simulation by Sala et al. [18], they analyzed the sensitivity of the cell performance to the geometric characteristics of the flow field. They showed that a wide channel is suitable for a low current density, and a narrow channel is suitable for a high current density. Mahmoudimehr et al. [19] by the numerical analysis of the single-channel fuel cells, showed the optimal geometry of the channels in various operating conditions. The results of their work showed that it was not possible to introduce constant dimensions that produce maximum output power in all the operating conditions.

It has been proved that the operating conditions have a considerable influence on the fuel cell performance [12,20–22]. Wang et al. [20] have experimentally investigated the effect of the operating characteristics such as the temperature, pressure, and relative humidity on the performance of the fuel cell. They revealed the positive effect of increasing humidity, temperature, and pressure on the performance. In an investigation, Acker Kahveci and Taymaz[21]have simulated a cell with a serpentine flow field. They studied the effects of the gas diffusion layer porosity, relative humidity, and operating pressure. The results obtained showed that the maximum power density was obtained by a porosity of 0.6, a relative humidity of 10% on the anode side, a relative humidity of 100% on the cathode side, and an operating pressure of 3 atm. Ghasabehi et al. [23] have presented a model for PEMFC based on its operating conditions. They optimized the operating conditions to reach a maximum power density that had a large amount and a high voltage. In a numerical study, Kane et al. [24]have applied the properties of a real air compressor. The results obtained showed that the power of the fuel cell and the power required by the compressor were directly related to the operating pressure of the system; in this study, 1.2 atm was introduced as the optimal pressure. In a paper given by Jawrungrit et al. [25], the pressure and temperature were analyzed. In this paper, they stated 3 atm and 393 K as the optimum values for the pressure and temperature, respectively.

PEMFCs as the propulsion systems of UAVs have attracted much attention [22,26–30]. Belmonte et al. [31]have investigated the implementation of a PEM fuel cell to extend the flying range of a drone for a mobile crane inspection. They showed that the selection between battery and fuel cell is mainly driven by a combination of costs and flying time requirements. Rostami et al. [26]have presented a model of a UAV propulsion system based on a combination of fuel cell and battery. Their findings revealed that by increasing the altitude, the performance of the propulsion system was greatly reduced. Gonzalez-Espasandín et al.[22]have studied the performance of fuel cell-driven UAVs. The voltage drop of the direct methanol fuel cell and proton exchange membrane fuel cell under the atmospheric conditions was demonstrated. Toghyani et al. have proposed a novel been-shaped flow field [27]. The novel flow

field enhanced the specific power of a PEMFC-powered UAV.

The main goal of this work is to improve the performance of the PEMFC propelled UAVs by an innovative flow field. In order to reach this goal, a modified combined flow field is presented, and compared with four flow fields including parallel, serpentine, interdigitated, combined. The effects of these flow fields on the reactant, water management, pressure drop, and specific power density are investigated and compared. Then the effect of the atmospheric flight conditions is studied under the modified combined flow field. To recapitulate, to reinforce performance of PEMFC-driven UAVs, an enhanced flow field is recommended, and two correlations for its performance under the flight conditions at low and high voltages are presented.

2. Computational domain

One of the main stages of this work aims to compare the performance of five flow fields including parallel, serpentine, interdigitated, combined, and modified combined. Therefore, in a two-phase 3D simulation, nine computational domains of PEMFC including bipolar plates, gas diffusion layers, catalyst layers, and membrane are studied. A schematic view of the flow fields is shown in figure 1. All flow fields comprise 2 main channels and 21 sub-channels. The operating conditions and the dimensions of the components are tabulated in tables 1 and 2, respectively. The described basic operating conditions and dimensions are regulated according to the atmospheric condition and references [12,27]. In the modified flow field, the main channels are tapered to reduce the pressure drop.

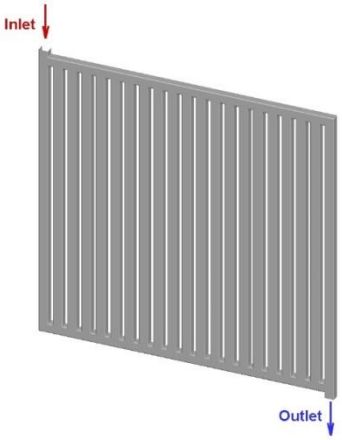

(a)

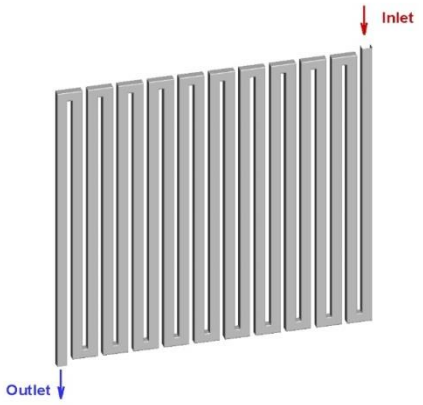

(b)

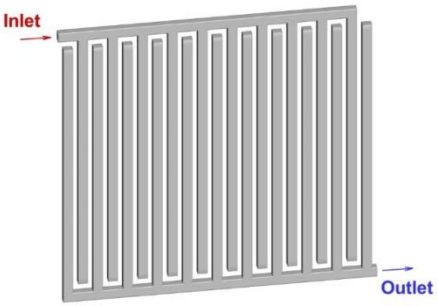

(c)

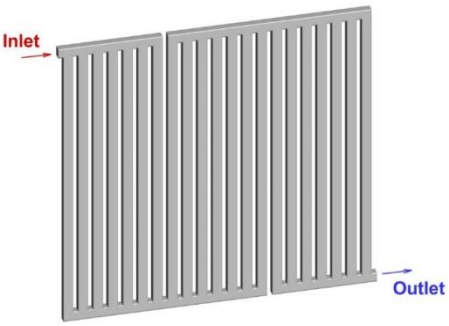

(d)

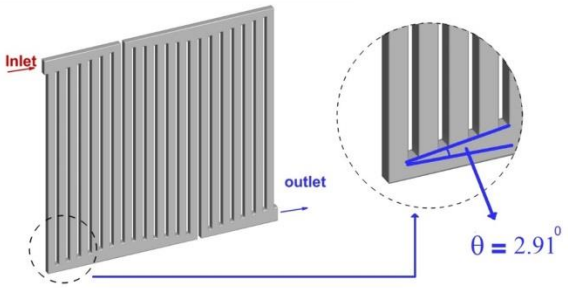

(e)

Figure 1. Flow fields (a) parallel (b) serpentine (c) interdigitated (d) combined (e) modified combined.

Table 1.Operating conditions.

Parameter	Value	Unit
Operating pressure P	101325	Pa
Cell temperature T	298	K
Anode relative humidity RH	75	%
Cathode relative humidity RH	75	%
Anode stoichiometry	1.85	
Cathode stoichiometry	2.5	

Table 2. Dimensions of components in simulated PEMFC.

Parameter	Value	Unit
Channel height	1.2	mm
Channel width	1.52	mm
Rib width	0.83	mm
BP thickness	2.4	mm
Cell active area	25	cm^2
GDL thickness	260	µm
CL thickness	10	µm
Membrane thickness	30	µm

3. Governing equations

The model of PEMFCs is a sophisticated multiple-physics coupling one. It is 3D, multi-phase, non-isothermal, and stable. The reactions (1) and (2) take place at the catalyst surface on both sides, respectively.

$$\mathbf{H_2 \rightarrow 2\,H^+ + 2\,e^-} \tag{1}$$

$$\mathbf{\frac{1}{2}O_2 + 2\,H^+ + 2\,e^- \rightarrow H_2O} \tag{2}$$

Equation (3) represents the continuity equation. The mixture density exerted in this equation is calculated by equation (4) [32].

$$\mathbf{\frac{\partial(\varepsilon\rho_{mix})}{\partial t} + \nabla\cdot(\varepsilon\rho\,\vec{u}) = S_m} \tag{3}$$

$$\mathbf{\rho_{mix} = \frac{P}{RT\sum\frac{Y_i}{M_i}}} \tag{4}$$

Where ε denotes the porosity of porous zones that is set to be 0 at the bipolar plate, ρ is the density of the species, and $\vec{u}$ is the velocity vector. Furthermore, the pressure, temperature, universal gas constant, molecular weight, and mass fraction are signed as P, T, R, M, and Y, respectively. Sm is a source term that is non-zero only in the catalyst zones on both sides. The general form of the momentum equation is shown in equation (5). The source term of this equation is non-zero only in CL and GDL [33].

$$\mathbf{\frac{\partial(\varepsilon\rho\vec{u})}{\partial t} + \nabla\cdot(\varepsilon\rho\,\vec{u}\vec{u}) = -\varepsilon\nabla P + \vec{\nabla}\cdot(\varepsilon\mu\nabla\,\vec{u}) + S_u} \tag{5}$$

The energy conservation equation in the solution domain can be calculated using the following equation:

$$\mathbf{\frac{\partial(\varepsilon\rho c_p T)}{\partial t} + \nabla\cdot(\rho\,c_p\vec{u}\,T) = \nabla\cdot(k_{eff}\,\nabla T) + S_T} \tag{6}$$

where k_{eff} is the effective thermal conductivity, c_p is the specific heat at a constant pressure, and S_T is the additional volumetric source term of energy equation.The reactants are hydrogen and air that are considered as ideal gases. These species transport equations and are described as follow:

$$\mathbf{\frac{\partial(\varepsilon C_i)}{\partial t} + \nabla\cdot(\varepsilon\,\vec{u}C_i) = \nabla\cdot\left(D_i^{eff}\nabla C_i\right) + S_i} \tag{7}$$

where C_i is the molar concentration of "i" species, andS_i is the additional volumetric source term of the species. Moreover, D_i^{eff} gas diffusivity coefficient, which is affected by operation condition, is given by[34]:

$$\mathbf{D_i^{eff} = \varepsilon^{0.5}(1-s)^{r_s}D_i^{ref}\left(\frac{P_0}{P}\right)\left(\frac{T}{T_0}\right)^{\frac{3}{2}}} \tag{8}$$

where $r_s$denotesthe saturation exponent of pore blockage, $D_i^{ref}$is the reference mass diffusivity of thei^{th} species at standard condition, and s is considered as water saturation or the volume fraction of liquid water, and calculated as follows:

$$\mathbf{S = \frac{Vol_{liquid}}{Vol}} \tag{9}$$

Generally, the volumetric transfer currents can be described by the Butler-Volmer equation, given by [20]:

$$\mathbf{j_a = (\xi_a j_a^{ref})_a\left(\frac{C_{H2}}{C_{H2}^{ref}}\right)^{\gamma_a}\left[\exp\left(\frac{\alpha_a F}{RT}\eta_a\right) - \exp\left(\frac{-\alpha_c F}{RT}\eta_a\right)\right]} \tag{10}$$

$$\mathbf{j_c = (\xi_c j_c^{ref})_c\left(\frac{C_{O2}}{C_{O2}^{ref}}\right)^{\gamma_c}\left[-\exp\left(\frac{\alpha_a F}{RT}\eta_c\right) + \exp\left(\frac{-\alpha_c F}{RT}\eta_c\right)\right]} \tag{11}$$

where j^{ref}, ξ, and α are the reference exchange current density, specific active surface area, and transfer coefficient, respectively. Also c, c_{ref} and γ represent the local species concentration of the reactant flow, reference value, and concentration dependence, respectively. The driving force behind the electrochemical reaction is the surface over potential, representing the difference

between the potentials of the solid and membrane phase; the electrochemical equations solved for the two potentials are expressed by:

$$\nabla \cdot (\sigma_{sol} \cdot \nabla \phi_{sol}) - j_{sol} = 0 \quad (12)$$

$$\nabla \cdot (\sigma_{mem} \cdot \nabla \phi_{mem}) + j_{mem} = 0 \quad (13)$$

where σ is the electrical conductivity and ϕ is the electrical potential. The subscribes sol and mem show the solid phase and electrolyte phase, respectively. j_{sol}andj_{mem}denotethe source terms that can be calculated using the following equations, respectively:

$$j_s = -j_a < 0 \qquad j_m = +j_a > 0 \quad (14)$$

Cathode side:

$$j_s = +j_c > 0 \qquad j_m = -j_c < 0 \quad (15)$$

The over-potential is solved as follows:

$$\eta_a = \phi_{sol} - \phi_{mem} \quad (16)$$

$$\eta_c = \phi_{sol} - \phi_{mem} - V_{OC} \quad (17)$$

In PEMFCs, especially at low potential regions, the water may condense and form liquid water resulting in blocking the GDL, and therefore, degradation of the cell performance. The present model of formation and transport of liquid water is based on the model of Nam and Kaviany[35], and Nguyen [36], as shown in equation (18). In this equation, the liquid phase velocity in the Gas Flow Channel (GFC) equals to the gas phase velocity.

$$\lambda = \begin{cases} 0.043 + 17.81a_w - 39.85a_w^2 + 36a_w^3 \; 0 < a_w \le 1 \\ 14 + 1.4(a_w - 1) \; 1 < a_w \le 3 \end{cases} \quad (19)$$

wherea_w is the water activity that is obtained using the following equation:

$$a_w = \frac{P_{wv}}{P_{sat}} + 2s \quad (20)$$

The protonic conductivity of the membrane can be calculated as a function of the membrane water content, as proposed by Springer et al. [37], given by:

$$\sigma_{mem} = [0.00514\,\lambda - 0.00326]\exp\left[1268\left(\frac{1}{303} - \frac{1}{T}\right)\right] \quad (21)$$

The osmotic drag coefficient n_d and water diffusivity in the membrane D_w are computed using equations 30 and 31, respectively.

$$n_d = 2.5\frac{\lambda}{22} \quad (22)$$

$$D_w = D_\lambda \exp\left[2416\left(\frac{1}{303} - \frac{1}{T}\right)\right]$$

$$D_\lambda = \begin{cases} 3.1 \times 10^{-7}\lambda(\exp(0.28\lambda) - 1)\exp\left(\frac{-2346}{T}\right) & 0 \le \lambda \le 3 \\ 4.17 \times 10^{-8}\lambda(161\exp(-\lambda) + 1)\exp\left(\frac{-2346}{T}\right) & \lambda > 3 \end{cases} \quad (23)$$

The source terms of the equations are given in table 3.

Table 3. Source terms of the equations.

Equation	Zone	Source term
Continuity	CL_a	$-\frac{j_a}{2F}M_{H_2}$
	CL_c	$-\frac{j_c}{4F}M_{O_2} + \frac{j_c}{2F}M_{H_2O}$
Chemical specious	CL	$S_{H_2} = -\frac{j_a}{2F}$
		$S_{O_2} = -\frac{j_c}{4F}$
		$S_{H_2O} = +\frac{j_c}{2F}$
Momentum	Porous zones	$S_u = \frac{-\mu}{K_p}\varepsilon\vec{u}$
Energy	CL andMem	$S_T = I^2R_{ohm} + h_{react} + \eta j_{a\,,c}$
Water saturation	Channels and Porous zones	$S_w = c_r max$ $[(1-s)\frac{P_{wv} - P_{sat}}{RT}M_{w-H_2O}$ and $-s\rho_1]$

The Response Surface Methodology (RSM) can be used to prepare a model between the objective and decision variables. A regression is carried out to relate the response, y, and the input parameters denominated by x_1, x_2, …,x_k, and in the form of the following equation:

$$y = \beta_0 + \sum_{i=1}^{j}\beta_i x_i + \sum\sum_{i<j}\beta_{ji}x_i x_j + \sum_{i=1}^{j}\beta_{ii}x_{ii}^2 + error \quad (24)$$

where β is a vector of constant coefficients. Simulations are designed by Central Composite Design (CCD) of RSM. It is done for different values of operating parameters including a temperature of 273–308K, and a pressure of 0.6–0.8 atm according to reference [22].

4. Simulation and validation

In the present investigation, PEMFC was simulated by computational fluid dynamics (CFD) in the ANSYS FLUENT software [38]. The governing equations used in this work include the continuity equation, momentum survival equations, energy conservation, species transfer equations, Butler-Volmer equation, and liquid water formation and transfer equations. Rhe simulations were performed in the stable, multi-phase, and non-isothermal conditions. The discretization of the equations was carried out using the finite volume method based on the Simple algorithm. The F-cycle technique and the BCGSM method were utilized in order to achieve an acceptable convergence. The residual magnitude of 10-4 was considered as the convergence criterion for all equations. Both the liquid and gas phases has the same velocities in the flow field. In the simulation, the transfer of water from the membrane was possible through electro-osmosis and diffusion, and the transverse flow of gas in the membrane was ignored. The porous properties of the electrodes and membrane were homogeneous and isotropic. The electrochemical reactions were considered as heterogeneous reactions, and the water produced by steam was in the vapor form and then condensed. The physical properties of PEMFC are summarized in table 4.

The computational grid in the present simulation had hexagonal elements reducing the distortion. The grid independency was checked by increasing the number of nodes. The current density for different computational grids with different numbers of elements including 4010651, 1944360, 710193, 350111, and 180324 were analyzed. Figure 2 (a) shows that according to the results of the sample simulation with 1944360, the elements were selected as the appropriate grid.

In order to evaluate the validity of the present numerical model, the polarization curve of reference[23]was compared with the present model. The geometry, operational conditions, and physical properties of the materials were the same in the simulation and the experiment. Figure 2 (b) shows an appropriate coherence between the simulation and the reference[23].

Table 4. Parameters used in the model.

Parameter	Value	Unit
Porosity of GDL	0.5	
Porosity of CL	0.5	
Thermal conductivity of GDL	10	W $m^{-1}K^{-1}$
Thermal conductivity of CL	10	W $m^{-1}K^{-1}$
Thermal conductivity of membrane	2	W $m^{-1}K^{-1}$
Thermal conductivity of current collector	100	W $m^{-1}K^{-1}$
Electrical conductivity of GDL	5000	Siemens m^{-1}
Electrical conductivity of CL	5000	Siemens m^{-1}
Electrical conductivity of membrane	1×10^{-16}	Siemens m^{-1}
Electrical conductivity of current collector	1,000,000	Siemens m^{-1}
Contact resistance between GDL/Bipolar	2×10^{-6}	Siemens m^{-1}
Contact angle anode/cathode	140	°
CL surface/volume ratio	200,000	m^{-1}
Membrane equivalent weight	1100	kg $kmol^{-1}$
Anode reference concentration	1	kmol m^{-3}
Cathode reference concentration	1	kmol m^{-3}
Anode reference current density	7500	A m^{-2}
Cathode reference current density	20	A m^{-2}
Open-circuit voltage V_{oc}	0.972	V

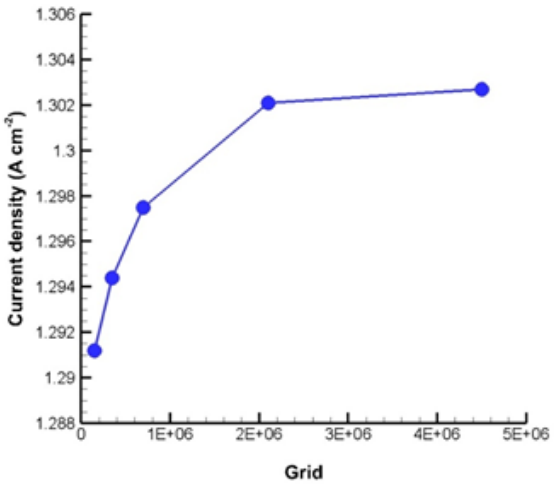

(b)

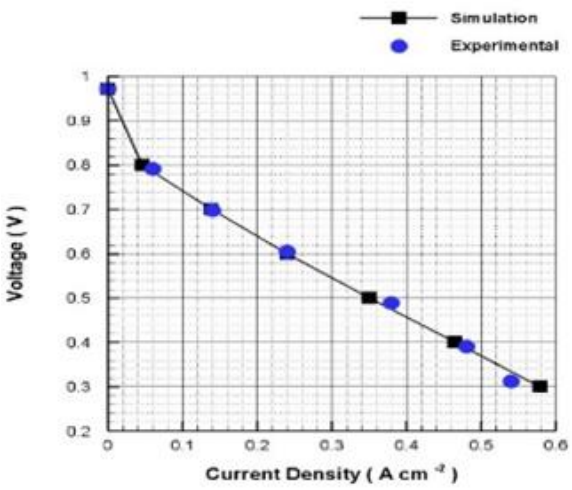

(c)

Figure 1. Simulation (a) grid independency and (b)validation.

4.2. Results

The results obtained consist of two main parts. First, five flow fields including parallel, serpentine, interdigitated, combined, and modified combined were compared, and their performance in the PEMFC was investigated. Then PEMFC was studied with the ideal flow field under the atmospheric flight conditions of UAVs.

5.1.1. Polarization curve

The polarization curve and the power density curve for parallel, serpentine, both combined cases, and interdigitated flow fields are shown in figure 3. Although parallel had the worst performance by a wide margin, there was atrivial difference between the other flow fields. Notwithstanding the minor difference, in an increasing maximum power density sequence, the flow fields are parallel by 0.535, interdigitated by 0.813, combined by 0.832, modified combined 0.839, and serpentine 0.851. The difference between the flow fields is more apparent at low voltages.

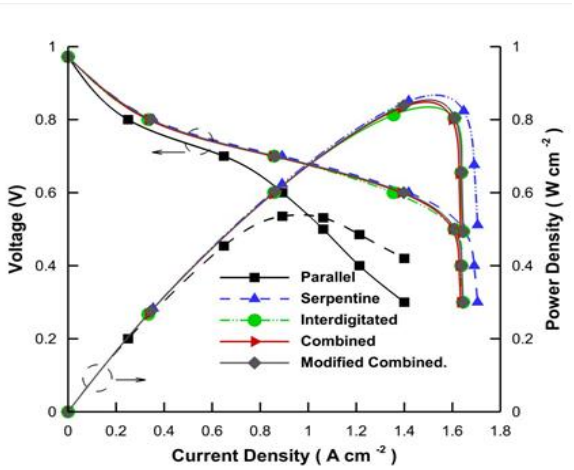

Figure 2. Performance of flow fields: polarization curve (left axis) power density (right axis).

5.1.2. Reactant distribution

The uniform distribution of oxygen on the catalyst results in a uniform reaction, and the lack of oxygen leads to a significant concentration over-potential. Figure 4 demonstrates the mass fraction of oxygen at the interface between the gas diffusion layer and the catalyst layer at a constant voltage of 0.6 V. It is apparent that in the serpentine and both combined cases, the mass fraction of oxygen continuously decreases as it approaches the outlet. Moreover, an area with a lack of oxygen is found beneath the central sub-channels of the parallel flow field. This area reduces the reaction rate, and the reduction is consistent with the reference results [12,23]. In the interdigitated flow field, the mass fraction of oxygen in the inlet sub-channels is greater than the output sub-channels.

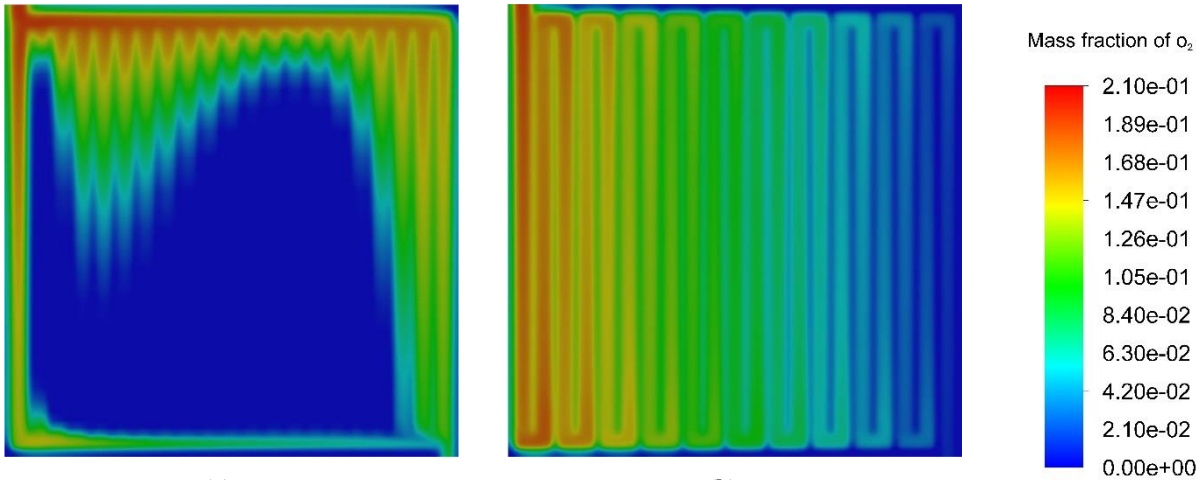

(a) **(b)**

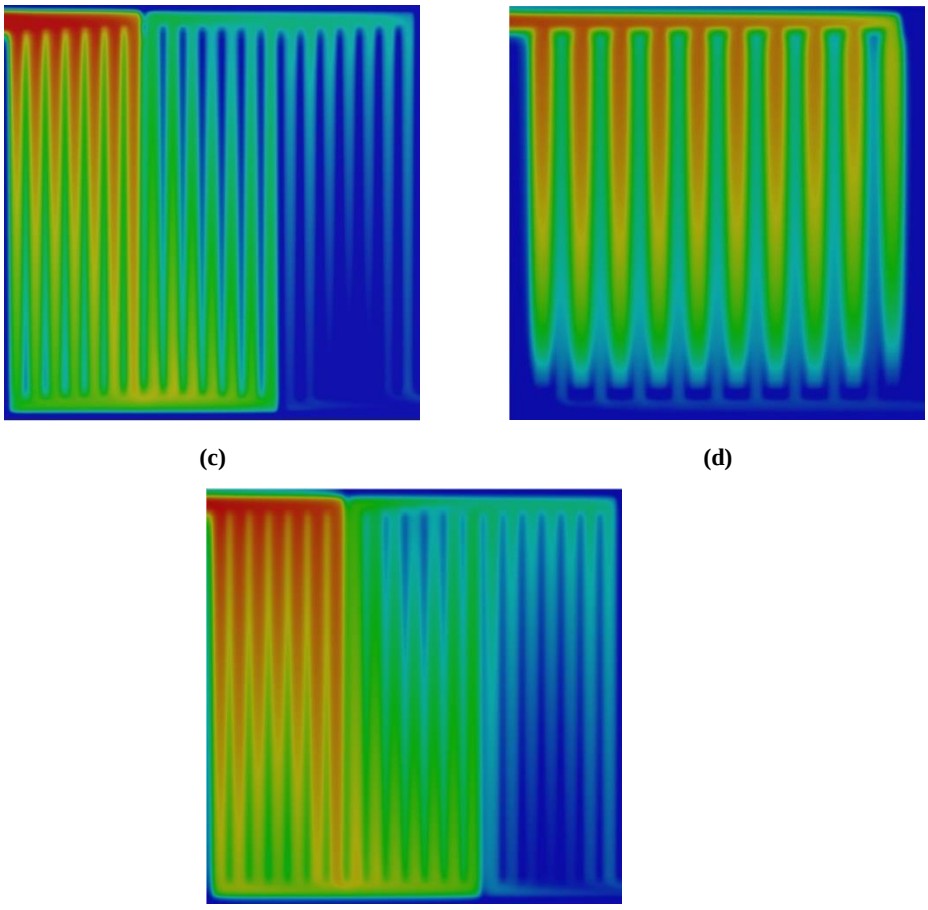

Figure 3. Distribution of oxygen mass fraction on the interface of the gas diffusion layer and catalyst layer at the cathode side in the flow fields (a) parallel (b) serpentine (c) interdigitated (d) combined (e) modified parallel flow field.

5.1.3. Water management

Water management includes the management of PEMFC in a way that the membrane is provided with enough water content and the possibility of flooding reduces. If the amount of water in the membrane increases, the condensation of water vapor and the formation of liquid water in the catalyst layer, gas diffusion layer, and channels lead to flooding in the cell. Figure 5 shows the distribution of water saturation over the interface of the gas diffusion layer and the catalyst layer. In a consistent behavior with oxygen distribution and references [39–42], the amount of water saturation increases along the channel of the serpentine and both combined case. The interdigitated flow field has a high water saturation, especially in the outlet sub-channels. The parallel flow field has a high water saturation, and the distribution of water saturation is completely non-uniform. Water removal in the parallel flow field and the interdigitated flow field is weak because the air velocity in these flow fields is low.

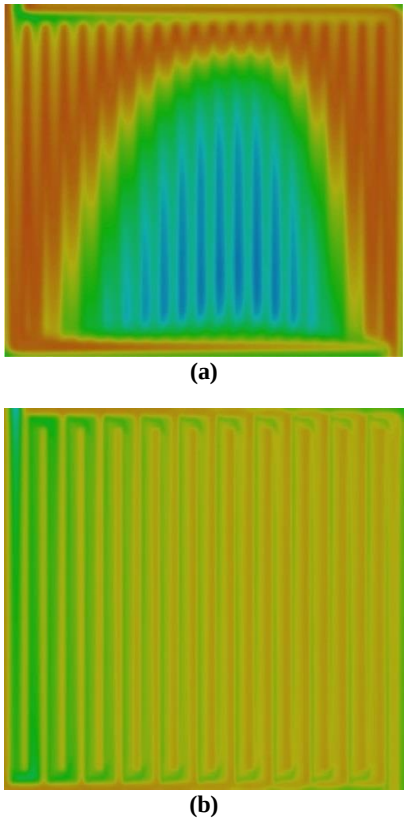

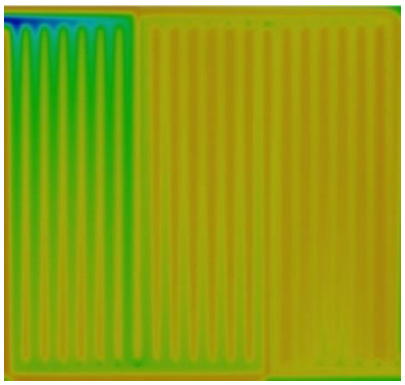

(c)

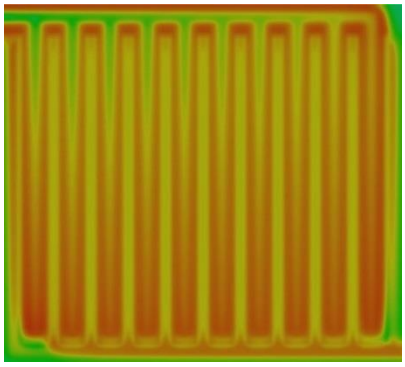

(d)

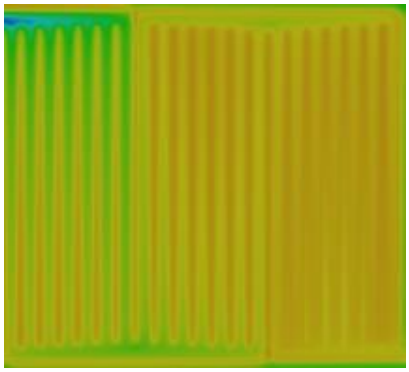

(e)

Figure 4. Distribution of water saturation over the interface of the gas diffusion layer and catalyst layer at the cathode side in the flow fields (a) parallel (b) serpentine (c) interdigitated (d) combined(e) modified parallel flow field.

If the amount of water content in the membrane decreases, the drying of the membrane will occur leading to a lower proton conduction and higher ohmic losses. Figure 6 shows the water content in the membrane. The membrane water content in the serpentine and both combined designs has a high uniformity, and these flow fields bring moderate amounts of water content. The results obtained show that the uniform distribution of the reactants in the flow field leads to the uniformity of the water content in the membrane. The water content under outlet sub-channels of the interdigitated flow is more than the other parts. There is a large area with low water content in the parallel design, while there is an arc-like area with a high water content around the area with low water content.

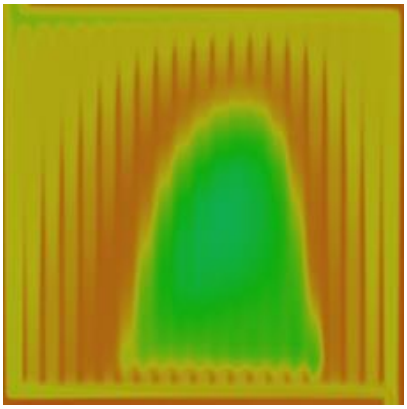

(a)

(b)

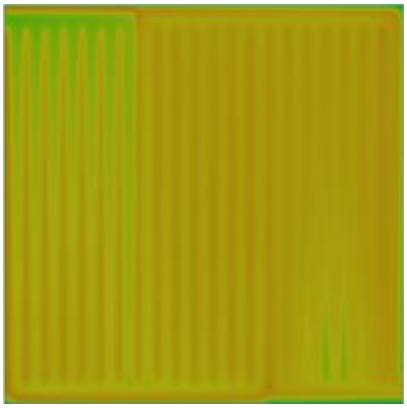

(c)

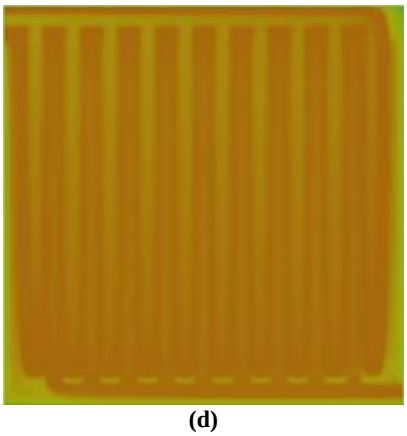

(d)

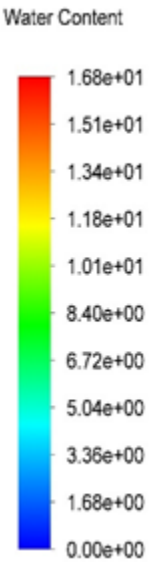

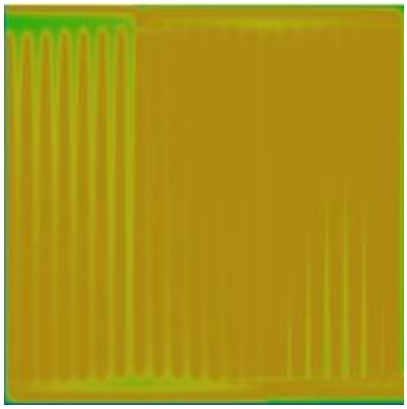

(e)

Figure 5. Distribution of water content within the membrane in the flow fields (a) parallel (b) serpentine (c) interdigitated (d) combined (e) modified parallel flow field.

5.1.4. Pressure drop

Reducing the pressure drop resulting in a lower power dissipation is of great significance to improve the overall efficiency of the cell. As shown in figure 7, the pressure drop in the serpentine and interdigitated flow fields is 2.493kPa and 0.964 kPa, respectively, which is significantly higher than the parallel and both combined flow fields. In the modified combined compared with simple combined, the pressure drop decreased to 22.6%.

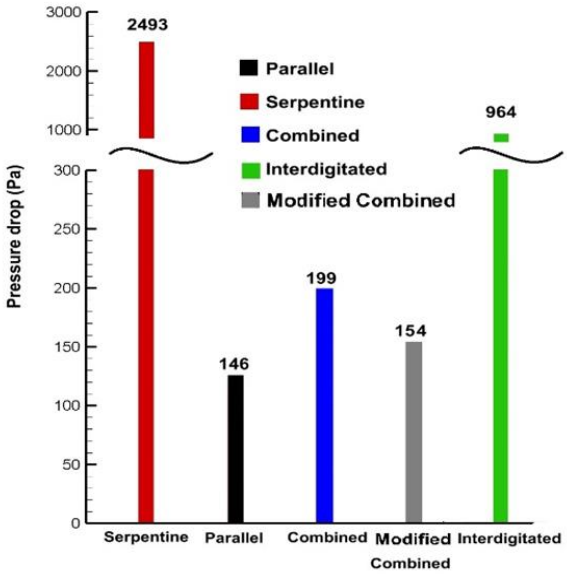

Figure 6. Pressure drop in flow fields.

5.1.4. Specific power

The flow fields have a key role in the performance of PEMFC. In this work, PEMFC as the propulsion system of a UAV with five flow fields including parallel, serpentine, interdigitated, combined, and modified combined was investigated. Each fuel cell or battery alone is not able to simultaneously support the three main parameters including high energy storage for flight endurance, high output power density required at take-off, and low weight. By combining these two systems, the main parameters can be achieved. The battery is used in the takeoff and climbing stages, and the PEMFC is employed in order to provide power and increase flight endurance in the cruise phase[43]. PEMFC is also used to recharge the battery during the cruise phase. The flight steps of a UAV and the time and power required for these steps are given in Table 5. In the present work, according to Table 5, the utilization of PEMFC in the cruise stage was investigated.

Table 5. Stack and battery discharge test mission profile [43].

Stage	Power
Standby position (waiting for takeoff)	2 min at 12 W
Takeoff	30 s at 800 W
Climb	2 min at 350 W
Cruise	2 h at 194 W
Landing	2 min at 12 W

More than half of the cell weight is related to the collector plates [44].In order to provide the required power for the cruise stage of UAV, it is necessary to calculate the number of fuel cell cells and their weight to form the cell mass. The weights of serpentine and interdigitated flow fields are less than the other two flow fields. The calculation of the number of cells required to provide the output power necessitated for the UAV propulsion system for an output power of 200 W is presented in table 6. This table shows that the modified combined flow field is an adequate option for a PEMFC powered UAV. The specific power of modified combined is 50% higher than the parallel, and it shows a slightly better performance than the other flow fields.

Table 6.Calculation of number and weight of fuel cells.

Flow field	**Number of cells**	**Weight of stack(kg)**	**Specific power (W kg^{-1})**
Serpentine	13	1.00	200.0
Parallel	19	1.46	137.1
Combined	13	0.98	203.77
Interdigitated	13	1.00	199.7
Modified combined	13	0.975	205.13

Overall, the modified combined is the ideal flow field due to its appropriate specific power density, suitable water management, and low pressure drop.

5.2. Atmospheric flight conditions

In this section, the effect of pressure and temperature coordinated with atmospheric flight conditions on the performance of modified combined PEMFC was investigated and optimized.

The interaction of pressure and temperature at a voltage of 0.7 V is demonstrated in figure 8. It is shown that the current density increases with increase in pressure, and the increase is accelerated in the middle range of temperature. Increasing the temperature from the minimum to the maximum causes an extreme point in the current density and power density. This process can be the result of the simultaneous effect of temperature in reducing saturated water and aggravating the membrane starvation [23]. The optimum temperature and pressure at 0.7 volts are 298.6 K and 0.8 atm, respectively, leading to a current density of 0.67A/cm2. At 0.4 V, the effect of pressure and temperature interaction on the output current density of the cell is presented in figure 9. The temperature dramatically affects the output current density. The increase in temperature decreases the liquid water resulting in a higher current density. The optimal values are 300.9 K and 0.75 atm leading to a power density of 1.75A/cm2.The output power density of PEMFC at low and high voltages are 0.7 W/cm2 and 0.47 W/cm2, respectively. Therefore, the output power density at the low voltage is 48.9% higher.

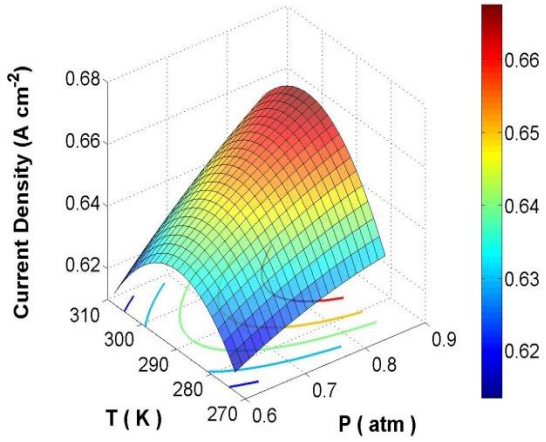

Figure7. Interaction of pressure and temperature at 0.7 V.

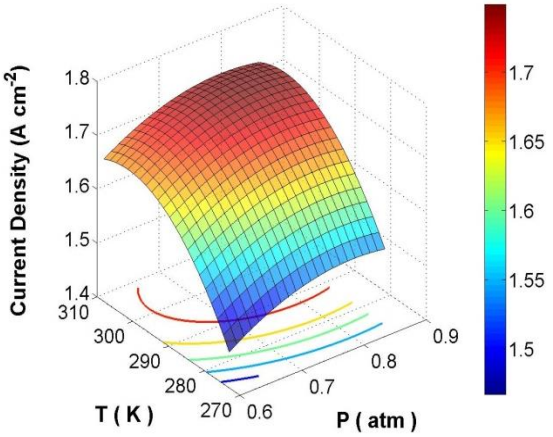

Figure 9. Interaction of pressure and temperature at 0.4 V.

Figure 10 shows the standardized effect of the operating conditions. This figure includes the effect of parameters on both low and high voltages. The results obtained indicate that temperature has a significant effect on the performance. The effect of temperature is more noticeable at a low voltage, and the effect of pressure is more important at a high voltage.

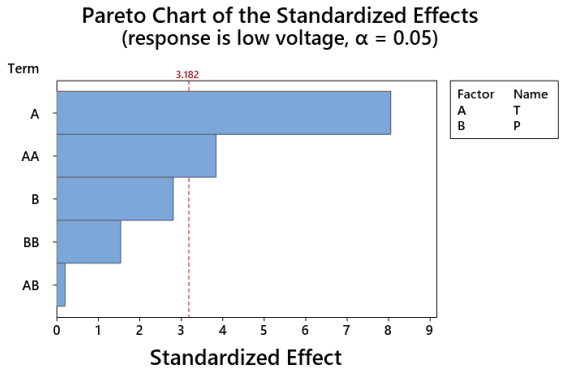

(a)

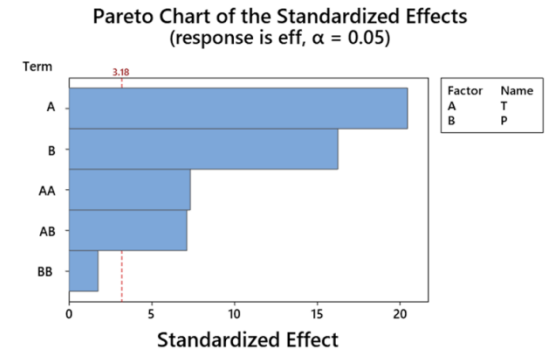

(b)

Figure 8. Effect of parameters on cell performance under (a) low voltage (b) high voltage.

Figure 8 and figure 9 show the interaction of pressure and temperature under low and high voltages, considering the possibility of the operating conditions coordinating. On the other

hand, the height of flight affects the operating conditions of the cell changing the output.
The International Standard Atmosphere (ISA) is a static atmospheric model of how the pressure and temperature of the Earth's atmosphere change over a wide range of altitudes. By gathering the data from the ISA and RSM methods, two equations (24 and25) are represented to predict the performance. The power in W/cm2 is related to the height in km at both low and high voltages. R-square is a statistical measure of how close the data is to the assumed regression line. R-square is 0.99, indicating the reliability of the equations.

$$\textbf{Power}\ (\mathbf{0.7\ v}) = \mathbf{4.73906 - 0.099028\ H - 0.014841\ H^2} \quad (25)$$

$$\textbf{Power}\ (\mathbf{0.4\ v}) = \mathbf{6.38859 + 0.22021\ H - 0.128494\ H^2} \quad (26)$$

At the low voltage, the concentration over-potential is dominant. Figure 11 shows the effect of flight altitude on the oxygen concentration at the reaction site. The data of this diagram is calculated by collecting the data from ISA and simulating PEMFC. Increasing the altitude reduces the oxygen concentration. Reducing the oxygen concentration at the reaction site can result in a lower current density.

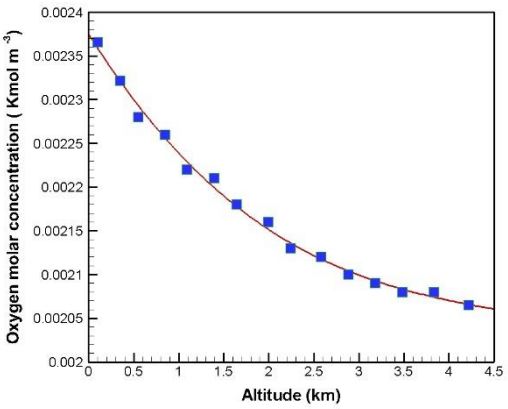

Figure9. Effect of altitude on oxygen concentration.

Figure 12 shows the changes in the power density under the atmospheric conditions. The decrease in height increases the output power at high altitudes, which is in full consistency with figure 11. According to figure 12, at the high voltage, PEMFC generates more output power, and at the low voltage, it has a relatively stable output power. If the flight altitude is constant, especially in the cruise phase, the low voltage is ideal. In a long-term decision and considering the issue of cell degradation in variable output power [45,46] and higher efficiency, the high voltage can be more suitable. At the high voltage, the desired power can be reached with more cells but dimensional limitations in the cell design must be considered.

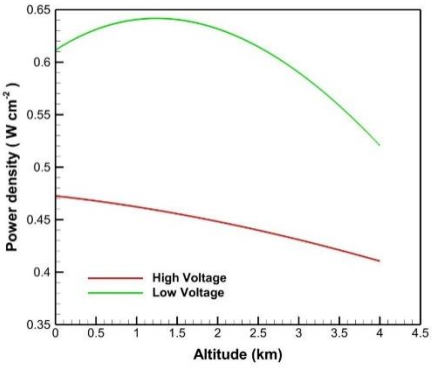

Figure 10. Effect of altitude on power density.

6. Conclusions

PEMFCs are employed as the propulsion systems in UAVs, especially at the cruise phase. Both the flow field and the operating conditions play pivotal roles in the performance. In this work, a modified combined flow field was introduced in order to enhance the performance of PEMFC-driven UAVs. First, the effect of the proposed flow field was investigated. Then the effect of altitude of UAV flight was studied. The following results were obtained:

1. In the modified combined flow field, the pressure drop was22.6% lower than the simple combined.
2. The modified combined provides a suitable water management and an appropriate oxygen distribution.
3. The specific power of modified combined, 205.13 W kg-1, is the highest value among all the flow fields.
4. Two equations were presented in order to predict the output power density at 0.4V and 0.7V in different flight attitudes.
5. The temperature dramatically affects the output current density. The optimum temperature and pressure at 0.7 volts are 298.6 K and 0.8 atm, leading to a power density of 0.47 W/cm2. At 0.4 V, the optimal values are 300.9 K and 0.75 atm, producing the power density of 0.7 W/cm2.
6. At a high flight altitude, the increase in height decreases the output current density, especially at the low voltage.
7. In the case of a constant flight altitude, especially in the cruise phase, the low voltage operation is better, and in the case of a long-term operation at variable altitudes, the high voltage can be more suitable.

7. References

[1] Stöcker C, Bennett R, Nex F, Gerke M, and Zevenbergen J. Review of the current state of UAV regulations. Remote Sens 2017;9. https://doi.org/10.3390/rs9050459.

[2] Pan ZF, An L, and Wen CY. Recent advances in fuel cells based propulsion systems for unmanned aerial vehicles. Appl Energy 2019;240:473–85. https://doi.org/10.1016/j.apenergy.2019.02.079.

[3] Adão T, Hruška J, Pádua L, Bessa J, Peres E, Morais R et al. Hyperspectral imaging: A review on UAV-based sensors, data processing, and applications for agriculture and forestry. Remote Sens 2017;9:1110.

[4] Zhang Q, Xu L, Li J, and Ouyang M. Performance prediction of proton exchange membrane fuel cell engine thermal management system using 1D and 3D integrating numerical simulation. Int J Hydrogen Energy 2018;43:1736–48. https://doi.org/10.1016/j.ijhydene.2017.10.088.

[5] Bao Z, Niu Z, and Jiao K. Analysis of single- and two-phase flow characteristics of 3-D fine mesh flow field of proton exchange membrane fuel cells. J Power Sources 2019;438:226995. https://doi.org/10.1016/J.JPOWSOUR.2019.226995.

[6] Toghyani S, Moradi Nafchi F, Afshari E, Hasanpour K, Baniasadi E, and Atyabi SA. Thermal and electrochemical performance analysis of a proton exchange membrane fuel cell under assembly pressure on gas diffusion layer. Int J Hydrogen Energy 2018;43:4534–45. https://doi.org/10.1016/j.ijhydene.2018.01.068.

[7] Mohammedi A, Sahli Y, and Ben Moussa H. 3D investigation of the channel cross-section configuration effect on the power delivered by PEMFCs with straight channels. Fuel 2020;263:116713. https://doi.org/10.1016/j.fuel.2019.116713.

[8] Wang X, Qin Y, Wu S, Shangguan X, Zhang J, and Yin Y. Numerical and experimental investigation of baffle plate arrangement on proton exchange membrane fuel cell performance. J Power Sources 2020;457:228034. https://doi.org/10.1016/j.jpowsour.2020.228034.

[9] Kahraman H and Orhan MF. Flow field bipolar plates in a proton exchange membrane fuel cell: Analysis andmodeling. Energy Convers Manag 2017;133:363–84. https://doi.org/10.1016/j.enconman.2016.10.053.

[10] Karanfil G. Importance and applications of DOE/optimization methods in PEM fuel cells: A review. Int J Energy Res 2020;44:4–25. https://doi.org/10.1002/er.4815.

[11] Afshari E, Ziaei-Rad M, and Dehkordi MM. Numerical investigation on a novel zigzag-shaped flow channel design for cooling plates of PEM fuel cells. J Energy Inst 2017;90:752–63. https://doi.org/10.1016/j.joei.2016.07.002.

[12] Ghasabehi M, Ashrafi M, and Shams M. Performance analysis of an innovative parallel flow field design of proton exchange membrane fuel cells using multiphysics simulation. Fuel 2021;285:119194. https://doi.org/10.1016/j.fuel.2020.119194.

[13] Duy VN, Lee J, Kim K, Ahn J, Park S, Kim T et al. Dynamic simulations of under-rib convection-driven flow-field configurations and comparison with experiment in polymer electrolyte membrane fuel cells. J Power Sources 2015;293:447–57. https://doi.org/10.1016/j.jpowsour.2015.05.107.

[14] Heidary H, Kermani MJ, and Dabir B. Influences of bipolar plate channel blockages on PEM fuel cell performances. Energy Convers Manag 2016;124:51–60. https://doi.org/10.1016/j.enconman.2016.06.043.

[15] Fan L, Niu Z, Zhang G, and Jiao K. Optimization design of the cathode flow channel for proton exchange membrane fuel cells. Energy Convers Manag 2018;171:1813–21. https://doi.org/10.1016/j.enconman.2018.06.111.

[16] Yang WJ, Wang HY, Lee DH, and Kim YB. Channel geometry optimization of a polymer electrolyte membrane fuel cell using genetic algorithm. Appl Energy 2015;146:1–10. https://doi.org/10.1016/j.apenergy.2015.01.130.

[17] Wang XD, Yan WM, Duan YY, Weng FB, Jung G Bin, and Lee CY. Numerical study on channel size effect for proton exchange membrane fuel cell with serpentine flow field. Energy Convers Manag 2010;51:959–68. https://doi.org/10.1016/j.enconman.2009.11.037.

[18] Sala P, Stampino PG, and Dotelli G. Design Approach for the Development of the Flow Field of Bipolar Plates for a PEMFC Stack Prototype. J Fuel Cell Sci Technol 2014;11:061003. https://doi.org/10.1115/1.4028150.

[19] Mahmoudimehr J and Daryadel A. Influences of feeding conditions and objective function on the optimal design of gas flow channel of a PEM fuel cell. Int J Hydrogen Energy 2017;42:23141–59. https://doi.org/10.1016/j.ijhydene.2017.07.196.

[20] Wang L, Husar A, Zhou T, and Liu H. A parametric study of PEM fuel cell performances. Int J Hydrogen Energy 2003;28:1263–72. https://doi.org/10.1016/S0360-3199(02)00284-7.

[21] Kahveci EE and Taymaz I. Assessment of single-serpentine PEM fuel cell model developed by computational fluid dynamics. Fuel 2018;217:51–8. https://doi.org/10.1016/j.fuel.2017.12.073.

[22] González-Espasandín Ó, Leo TJ, Raso MA, and Navarro E. Direct methanol fuel cell (DMFC) and H2 proton exchange membrane fuel (PEMFC/H2) cell performance under atmospheric flight conditions of Unmanned Aerial Vehicles. Renew Energy 2019;130:762–73. https://doi.org/10.1016/j.renene.2018.06.105.

[23] Ghasabehi M, Shams M, and Kanani H. Multi-objective optimization of operating conditions of an enhanced parallel flow field proton exchange membrane fuel cell. Energy Convers Manag 2021;230:113798. https://doi.org/10.1016/j.enconman.2020.113798.

[24] Qin Y, Du Q, Fan M, Chang Y, and Yin Y. Study on the operating pressure effect on the performance of a proton exchange membrane fuel cell power system. Energy Convers Manag 2017;142:357–65. https://doi.org/10.1016/j.enconman.2017.03.035.

[25] Jawrungrit C, Sirivat A, and Siemanond K. Improving proton exchange membrane efficiency of fuel cell by numerical simulation and optimization. Comput Aided Chem Eng 2016;38:1887–92. https://doi.org/10.1016/B978-0-444-63428-3.50319-2.

[26] Rostami M, Dehghan Manshadi M, and Afshari E. Performance evaluation of two proton exchange membrane and alkaline fuel cells for use in UAVs by investigating the effect of operating altitude . Int J Energy Res 2021:1–16. https://doi.org/10.1002/er.7263.

[27] Toghyani S, Atyabi SA, and Gao X. Enhancing the Specific Power of a PEM Fuel Cell Powered UAV with a Novel Bean-Shaped Flow Field. Energies 2021;14:2494. https://doi.org/10.3390/en14092494.

[28] Seo S-HH, Choi J-II, and Song J. Secure Utilization of Beacons and UAVs in Emergency Response Systems for Building Fire Hazard. Sensors 2017;17:2200. https://doi.org/10.3390/s17102200.

[29] Dyantyi N, Parsons A, Barron O, and Pasupathi S. State of health of proton exchange membrane fuel cell in aeronautic applications. J Power Sources 2020;451:227779. https://doi.org/10.1016/j.jpowsour.2020.227779.

[30] Boukoberine MN, Zhou Z, and Benbouzid M. A critical review on unmanned aerial vehicles power supply and energy management: Solutions, strategies, and prospects. Appl Energy 2019;255:113823. https://doi.org/https://doi.org/10.1016/j.apenergy.2019.113823.

[31] Belmonte N, Staulo S, Fiorot S, Luetto C, Rizzi P, and Baricco M. Fuel cell powered octocopter for inspection of mobile cranes: Design, cost analysis and environmental impacts. Appl Energy 2018;215:556–65. https://doi.org/https://doi.org/10.1016/j.apenergy.2018.02.072.

[32] Yuan W, Tang Y, Pan M, Li Z, and Tang B. Model prediction of effects of operating parameters on proton exchange membrane fuel cell performance. Renew Energy 2010;35:656–66. https://doi.org/10.1016/j.renene.2009.08.017.

[33] Atyabi SA and Afshari E. Three-dimensional multi-phase model of proton exchange membrane fuel cell with honeycomb flow field at the cathode side. J Clean Prod 2019;214:738–48. https://doi.org/10.1016/j.jclepro.2018.12.293.

[34] Um S, Wang C-Y, and Chen KS. Computational Fluid Dynamics Modeling of Proton Exchange Membrane Fuel Cells. Vol. 147. 2000.

[35] Nam JH and Kaviany M. Effective diffusivity and water-saturation distribution in single- and two-layer PEMFC diffusion medium. Int J Heat Mass Transf 2003;46:4595–611. https://doi.org/10.1016/S0017-9310(03)00305-3.

[36] Van Nguyen T. Modeling two-phase flow in the porous electrodes of proton exchange membrane fuel cells using the interdigitated flow fields. Proc-Electrochem Soc 1999;99–14:222–41.

[37] Springer TE, Zowodzinski TA, and Gottesfeld S. Polymer Electrolyte Fuel Cell Model. J Electrochem Soc 1991;138:2334–42. https://doi.org/10.1149/1.2085971.

[38] Fluent A. Theory Guide 17.2. Ansys Inc USA 2016.

[39] Bozorgnezhad A, Shams M, Kanani H, Hasheminasab M, and Ahmadi G. Two-phase flow and droplet behavior in microchannels of PEM fuel cell. Int J Hydrogen Energy 2016;41:19164–81. https://doi.org/10.1016/j.ijhydene.2016.09.043.

[40] Bozorgnezhad A, Shams M, Kanani H, Hasheminasab M, and Ahmadi G. The experimental study of water management in the cathode channel of single-serpentine transparent proton exchange membrane fuel cell by direct visualization. Int J Hydrogen Energy 2015;40:2808–32. https://doi.org/10.1016/j.ijhydene.2014.12.083.

[41] Kanani H. Experimental Investigation of Flooding in the Cathode Channels of the Polymer Exchange Membrane Fuel Cells. K. N. Toosi University of Technology, 2015.

[42] Anderson R, Zhang L, Ding Y, Blanco M, Bi X, and Wilkinson DP. A critical review of two-phase flow in gas flow channels of proton exchange membrane fuel cells. J Power Sources 2010;195:4531–53. https://doi.org/10.1016/j.jpowsour.2009.12.123.

[43] Lapeña-Rey N, Blanco JA, Ferreyra E, Lemus JL, Pereira S, and Serrot E. A fuel cell powered unmanned aerial vehicle for low altitude surveillance missions. Int J Hydrogen Energy 2017;42:6926–40. https://doi.org/https://doi.org/10.1016/j.ijhydene.2017.01.137.

[44] Li X, Sabir I. Review of bipolar plates in PEM fuel cells: Flow-field designs. Int J Hydrogen Energy 2005;30:359–71. https://doi.org/10.1016/j.ijhydene.2004.09.019.

[45] Ferreira RB, Falcão DS, and Pinto AMFR. Simulation of membrane chemical degradation in a proton exchange membrane fuel cell by computational

fluid dynamics. Int J Hydrogen Energy 2020. https://doi.org/10.1016/j.ijhydene.2020.09.179.

[46] LaConti AB, Hamdan M, and McDonald RC. Mechanisms of membrane degradation. Handb Fuel Cells2010. https://doi.org/10.1002/9780470974001.f303055.